Dislocations as natural quantum wires in diamond

Sevim Polat Genlik [ORCID],[*] Roberto C. Myers, and Maryam Ghazisaeidi[†]
Department of Materials Science at The Ohio State University, Columbus, Ohio 43210, USA

We study the electronic properties of the glide set of dislocations in diamond from first principles using hybrid exchange correlation functionals and find that the atomic-scale dislocation core states give rise to a prototypical one-dimensional (1D) band structure, i.e., natural quantum wires. The position and character of the core states varies strongly with local structure, where mixed dislocations with dangling bonds exhibit a 1D metallic band with a characteristic 1D density of states ($1/\sqrt{E}$). This 1D Fermi gas is spatially localized to a single atomic diameter orbital chain along the dislocation core. When the dangling bonds within the core are reconstructed, the 1D metallic band disappears. In contrast, pure edge dislocations in diamond reveal a 1D semiconductor with a direct band gap of 3.21 eV. These calculations provide a possible explanation to the long-standing observation of a blue luminescence band correlated with dislocations in diamond. This opens the door to using dislocations as 1D quantum phases with functional (electronic and optical) properties arising from the atomic-scale core states.

I. INTRODUCTION

Low-dimensional quantum materials have attracted significant attention because of their distinct properties from bulk. Despite extensive research on low-dimensional materials, major challenges in using them remain related to their fabrication and storage [1]. Dislocations—one-dimensional (1D) defects in crystals—are similar to low-dimensional materials, in the sense that the different bonding environment at their core leads to local and distinct properties from those in their surrounding crystal. They can be used as templates for creating conducting nanowires in insulating materials [2–5] or ferromagnetic nanowires in antiferromagnetic materials [6]. Moreover, dislocations are embedded in the solid, and as such are environmentally protected by their host. This is in contrast to existing low-dimensional quantum materials, such as metallic or semiconducting nanowires, which degrade in short time due to their instability [7].

Research on the effects of dislocations on the electronic properties of semiconductors dates back to 1953. First, Shockley reported that dangling bonds at the core of dislocations in germanium (Ge) and silicon (Si) should give rise to levels lying in the forbidden band gap [8]. Later, Read created a model for defect states, which assumed dislocations in Ge as acceptor type [9]. Another model proposed by Labusch and Schröter claimed that 1D defect states could be acceptor or donor type [10]. Even though dislocations in simple tetrahedrally bonded semiconductors (Si, Ge, etc.) have been investigated by a variety of theoretical and experimental methods [11–14], no unique and explicit model for the electronic states associated with dislocations in the band gap is adapted. For more than 40 years, most efforts to get insight into the

position of dislocation states in the gap resulted in ambiguity [15]. The main challenges in the analysis and interpretation of experimental data were attributed to the presence of networks of various type of dislocations, kinks and jogs, deformation-induced point defects, and the ubiquitous interaction between dislocations and point defects [15,16]. On the other hand, theoretical calculations could not clarify inconsistent experimental data because of once-limited computational power and finite size effects. Most theoretical researchers concluded their work by highlighting that correct positioning of defect levels can only be determined using realistic Hamiltonians and large numbers of atoms in calculations [17–20].

Despite the fair amount of work produced in the past, there is still a lack of complete understanding of the electronic properties of dislocations in elemental semiconductors. Recently, thanks to increases in computing power [21] and modern electronic density functional theory (DFT) codes, first-principles calculations of dislocations, using realistic functionals and large simulation systems, are now possible [22,23]. Here, we present a systematic first-principles study of partial dislocations in diamond with accurate positioning of their energy levels with respect to the host crystal's band structure. The electronic band structure of dislocations as well as the anisotropic carrier mobility in directions parallel and perpendicular to the dislocation line are calculated. The results show that metallic and semiconducting dislocations arise in diamond. 1D metallic bands are revealed within the core of unreconstructed (30°) partial dislocations, with a characteristic 1D density of states ($1/\sqrt{E}$). This 1D Fermi gas is spatially localized at a single-atom-wide p_z orbital chain along the dislocation line. In contrast, unreconstructed pure edge dislocations in diamond are 1D semiconductors with a direct band gap of 3.21 eV. Interband transitions within the latter theoretically explain the origin of the blue band luminescence in diamond, which the literature widely report to be correlated with dislocations [24–28]. These results prove that it is the

*polatgenlik.1@osu.edu
†ghazisaeidi.1@osu.edu

core states of the dislocations themselves in diamond that give rise to functional (electrical and optical) properties, rather than their distortion of the surrounding bulk diamond states. This opens the door to considering dislocations as 1D quantum phases.

In the rest of this paper, we first describe the computational setup. Next, we report the energetics of all calculated core configurations, as well as the ground state electronic properties of each configuration obtained using realistic hybrid functionals. Finally, carrier effective masses are calculated and discussed.

II. COMPUTATIONAL METHODS

DFT calculations are performed with the Vienna *ab initio* Simulation Package (VASP) [29] using projector augmented wave pseudopotentials [30]. Exchange correlations are treated by hybrid functionals with a Hartree-Fock mixing parameter α of 0.18 parametrized by Heyd, Scuseria, and Ernzerhof [31] to eliminate the band gap underestimation problem of DFT. Incorporating a 0.18 fraction of Hartree-Fock exchange recovered underestimation from 4.10 to 4.95 eV within the limits of computational resources. A plane-wave cut-off energy of 550 eV is used with a k-point density of 0.1 Å^{-1} for structural relaxations. Full periodic boundary conditions are used with a quadrupolar arrangement of dislocations using a triclinic simulation cell containing two dislocations with opposite Burgers vectors. The simulation cell consists of 576 atoms with a separation of ≈ 20 Å between the two dislocations and is oriented along $[\bar{1}\,\bar{1}\,2]$, $[1\,1\,1]$, and $[1\,\bar{1}\,0]$ corresponding to the x, y, and z directions, respectively. Two sets of supercells with single and double lattice translation periods are used along the $[1\,\bar{1}\,0]$ dislocation line direction to study core reconstruction.

The predominant slip system in the diamond cubic crystals is $\{111\}\langle 110\rangle$. A dislocation is titled as glide (shuffle) when slip takes place between closely (widely) spaced $\{111\}$ planes. We only consider the glide set of dislocations since they are glissile (capable of gliding) and the most stable [32]. The dislocations are introduced by displacing all atoms according to the elastic displacement field of the corresponding dislocation using anisotropic elasticity theory [33]. All atomic positions are subsequently optimized until forces are smaller than 10 meV/Å^{-1}.

To be able to directly compare the defective and perfect (bulk) simulation cells, the electrostatic potential in these cells need to be aligned [34] via

$$E_{\text{VBM}} = E_{\text{VBM}}^{\text{Perfect}} + V_{\text{av}}^{\text{Bulklike}} - V_{\text{av}}^{\text{Perfect}}.$$

Here, E_{VBM} and $E_{\text{VBM}}^{\text{Perfect}}$ correspond to the valence band maximum of the defective and the perfect cell, respectively, $V_{\text{av}}^{\text{Bulklike}}$ is the average potential in the bulklike region of the defective cell and $V_{\text{av}}^{\text{Perfect}}$ is the average potential of the perfect cell. The alignment procedure eliminates the shifts due to an arbitrary choice of zero average potential in DFT and correctly positions all the VBMs obtained from different calculations to a common reference position; in this case, $E_{\text{VBM}}^{\text{Perfect}}$. In the defective cell, atoms with volumetric strain values smaller than 10^{-4} are considered bulklike and are used to compute $V_{\text{av}}^{\text{Bulklike}}$. For obtaining the band structure along the $[\bar{1}\,\bar{1}\,2]$ direction, band unfolding is performed with the

TABLE I. Energy difference between the reconstructed and unreconstructed partial dislocations obtained by allowing double lattice periodicity (DP) and single lattice periodicity (SP) along the line direction.

	$(E^{\text{DP}} - E^{\text{SP}})/\text{atom}$ (eV)
30° Shockley partial	−0.046
90° Shockley partial	−0.025

fold2Bloch code using 15 equidistant k points [35]. Effective mass calculations were performed with curve fitting and the finite difference method.

III. RESULTS AND DISCUSSION

Previous studies [36,37] compared the relative stability of the glide set of dislocations in diamond and suggested that dissociation of the 60° glide dislocation into 90° and 30° Shockley partials lying on the same $\{1\,1\,1\}$ glide plane is energetically favored. Therefore, we only investigate the electronic structure of Shockley partials with two types of reconstruction, i.e., "single period" (SP) and "double period" (DP), in this paper. We do not consider higher orders of periodicity reconstructions since doubling the period eliminated all the dangling bonds at the core region.

Table I presents the energy per atom for different relaxed dislocation core configurations. The corresponding relaxed core configurations are shown in Fig. 1. SP 30° partial dislocations have dangling bonds at their core as shown in Fig. 1(a). Doubling the lattice periodicity along the dislocation line allows for pairing dangling bonds of every second atom with their neighbors [Fig. 1(b)] and reduces the energy by 46 meV/atom. In the case of the 90° partial dislocation, all the core atoms in both DP and SP dislocations are fourfold coordinated with highly distorted bonds as shown in Figs. 1(c) and 1(d). Although no dangling bonds occur in either type of dislocation, the DP configuration is more favorable than the SP by ~25 meV/atom. The bonds are up to 15% stretched in the SP configuration and up to 11% stretched in the DP configuration with respect to the relaxed C-C bond length (1.54 Å) in perfect bulk diamond. Thus, strain in the SP core is released through the bond rearrangement, enhancing the stability of DP 90° partials. The small energy differences between the SP and DP glide set of dislocations imply that the structure adopted (DP or SP) can be altered depending on the environment, for example, by local strains, doping, or thermal excitation. Therefore, we consider all of these core configurations for electronic structure calculations. Next, we study the dislocation band structures and analyze the correlation between their electronic properties and core geometries. The electronic structure of defect-free diamond in an oblique cell configuration, comparable to dislocation supercells, is used as the reference.

Figures 2(a)–2(c) present the electronic band structures obtained along the dislocation line direction $[1\,\bar{1}\,0]$ for the reference and 30° dislocation dipole supercells. Our results reveal defect related states in DP 30° are localized and located rather close to the conduction band (CB) edge in comparison
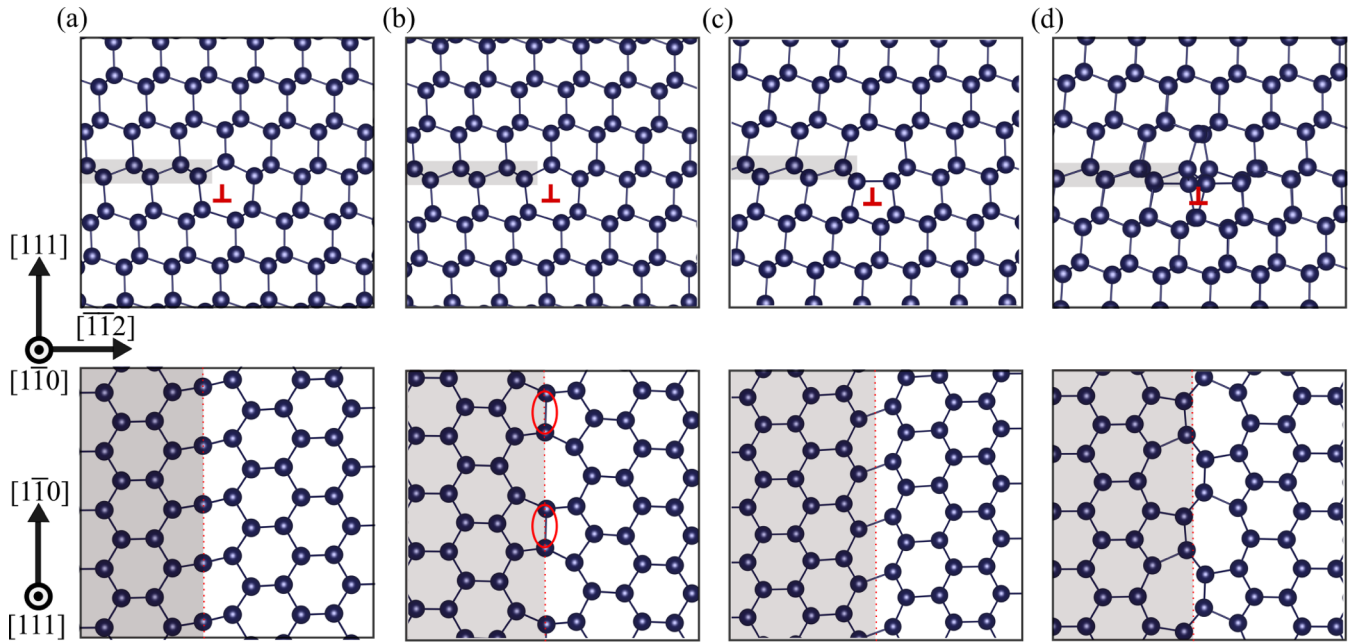
FIG. 1. Relaxed dislocation core structures of the glide set of Shockley partials in diamond. The relaxed core structure of (a) single period 30°, (b) double period 30°, (c) single period 90°, and (d) double period 90° Shockley partial dislocations. For each structure, the top figures show the top view of the $(1\bar{1}0)$ plane and the bottom figures show the $(1\,1\,1)$ glide plane. The stacking fault region associated with each partial is shaded. The location of dislocations on the top figures are marked with a red $\perp$ sign. The new bonds formed during core reconstruction are marked by red ellipses. Reconstructed bonds are showed in red circles for double period 30° type.
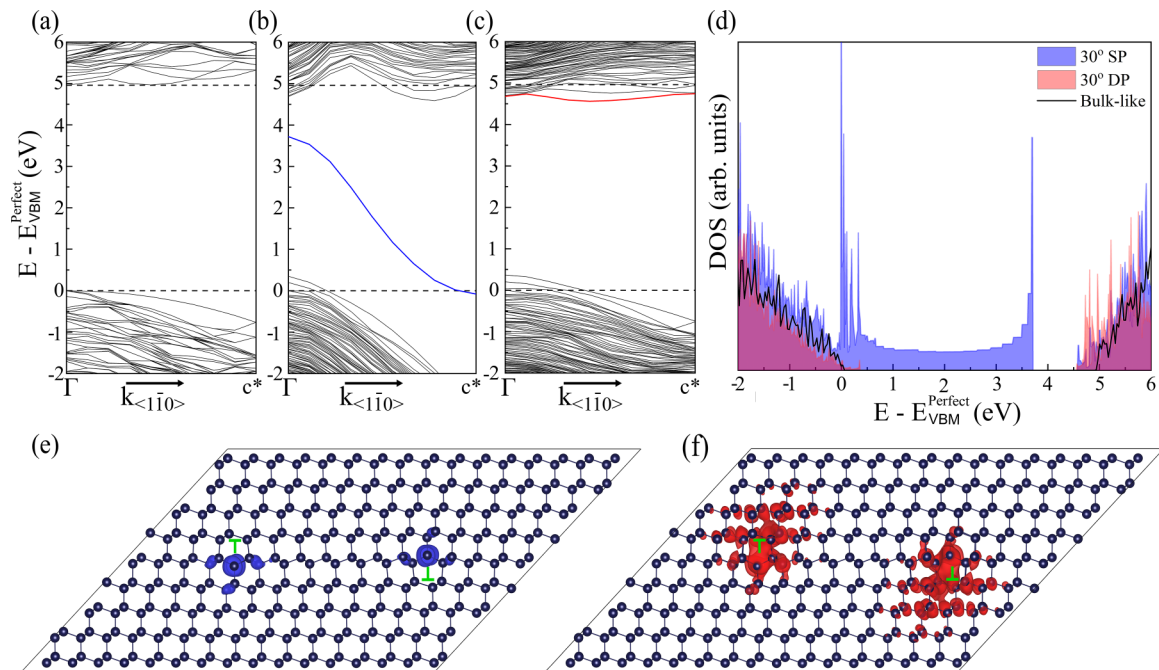

FIG. 2. Calculated electronic band structures along the dislocation line direction $[1\,\bar{1}\,0]$ for (a) the reference perfect (defect-free) supercell, and the supercell with (b) SP 30° and (c) DP 30° Shockley partial dislocation dipoles. (d) Calculated total electronic density of states for SP and DP 30° dislocation dipole supercells in reference to the perfect supercell. Band decomposed charge density distributions for (e) the blue colored deep defect level in the band structure of the SP 30° dislocation dipole supercell and (f) the red colored shallow defect level in the DP 30° dislocation dipole supercell. Locations of dislocation dipoles on figures are marked with green $\perp$ and $\top$ signs. Dashed lines on each panel show the conduction band minimum and the valence band maximum of the perfect bulk diamond as a reference.
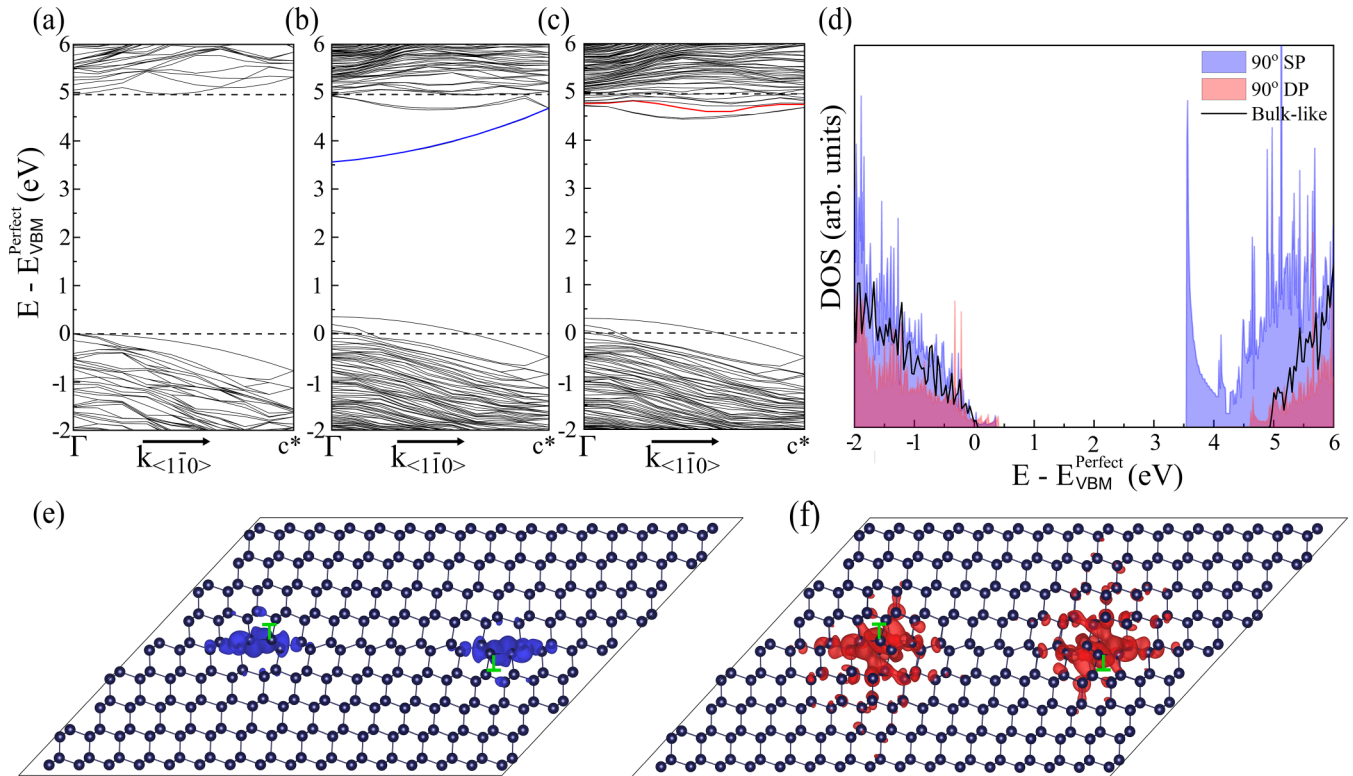
FIG. 3. Calculated electronic band structures along the dislocation line direction $[1\bar{1}0]$ for (a) the reference perfect (defect-free) supercell, and the supercell with (b) SP 90° and (c) DP 90° Shockley partial dislocation dipoles. (d) Calculated total electronic density of states for SP and DP 90° dislocation dipole supercells in reference to the perfect supercell. Band decomposed charge density distributions for (e) the blue colored deep defect level in SP 90° dislocation dipole supercell and (f) the red colored shallow defect level in DP 90° dislocation dipole supercell. Locations of dislocation dipoles on figures are marked with green ⊥ and ⊤ signs. Dashed lines on each panel show the conduction band minimum and the valence band maximum of the perfect bulk diamond as a reference.

to defect states in SP 30°. On the other hand, the SP 30° partial gives rise to an extremely broad defect state overlapping with the valence band and extended through the gap up to the proximity of the conduction band due to a row of dangling bonds propagating along the dislocation line. These midgap states are found to be half filled, which implies both acceptor and donor activity is possible depending on the position of the Fermi level. Disappearance of the midgap states in the DP reconstruction is attributed to the elimination of these dangling bonds. It should also be noted that two degenerate defect states are observed in each case due to the existence of two dislocations in the supercell.

Density of states (DOS) plots are shown in Fig. 2(d), revealing that the presence of dislocations gives rise to not only a defect state in the gap region but also shifts in the valence and CB edges for the SP 30° partial. Moreover, the atomic origins of induced defect states are investigated through band decomposed charge density analysis [Figs. 2(e) and 2(f)], with the defect states and corresponding partial charge densities color-coded. It is evident that these states are located in the dislocation core region, and that the degree of spatial localization for the SP 30° reconstruction is larger than that of the DP 30°.

Figures 3(a)–3(d) exhibit that neither the SP nor the DP reconstructions in 90° partial dislocations induce midgap states well separated from the valence band (VB) and CB edges of

bulk diamond. However, the SP 90° core, with higher strain, gives rise to a relatively dispersive conduction band compared to the DP 90°. Similar to the case of the 30° dislocations, the decomposed partial charge densities show that the dislocation states are localized around their core regions in real space [Figs. 3(e) and 3(f)]. This observation is consistent with the fact that localized defect states are created by dangling bonds which are absent in either structure of the 90° partial dislocations.

Notice that the top of the valence band edges are shifted to higher energy levels for both the 30° and 90° partials in comparison to the bulk diamond reference [Figs. 2 and 3(a)–3(c)]. We found that these shifted bands are occupied and localized around the stacking fault region between the two dislocations.

We also calculate the band structure along the x direction ($[\bar{1}\bar{1}2]$), which is perpendicular to the dislocation line. Band folding effects arise in this case due to having more than one lattice translation along the x direction of the $8 \times 1 \times 1$ supercell. Note that, in the case of DP supercells, the double periodicity is considered as the new translation vector along the line due to reconstruction.

Figure 4 shows the unfolded band structures. Because the position of the valence and conduction band edges are affected by folding along the x direction, we unfolded all the band structures for comparison. For SP 30° partials, dispersionless electronic states (i.e., flat bands) are observed along the x
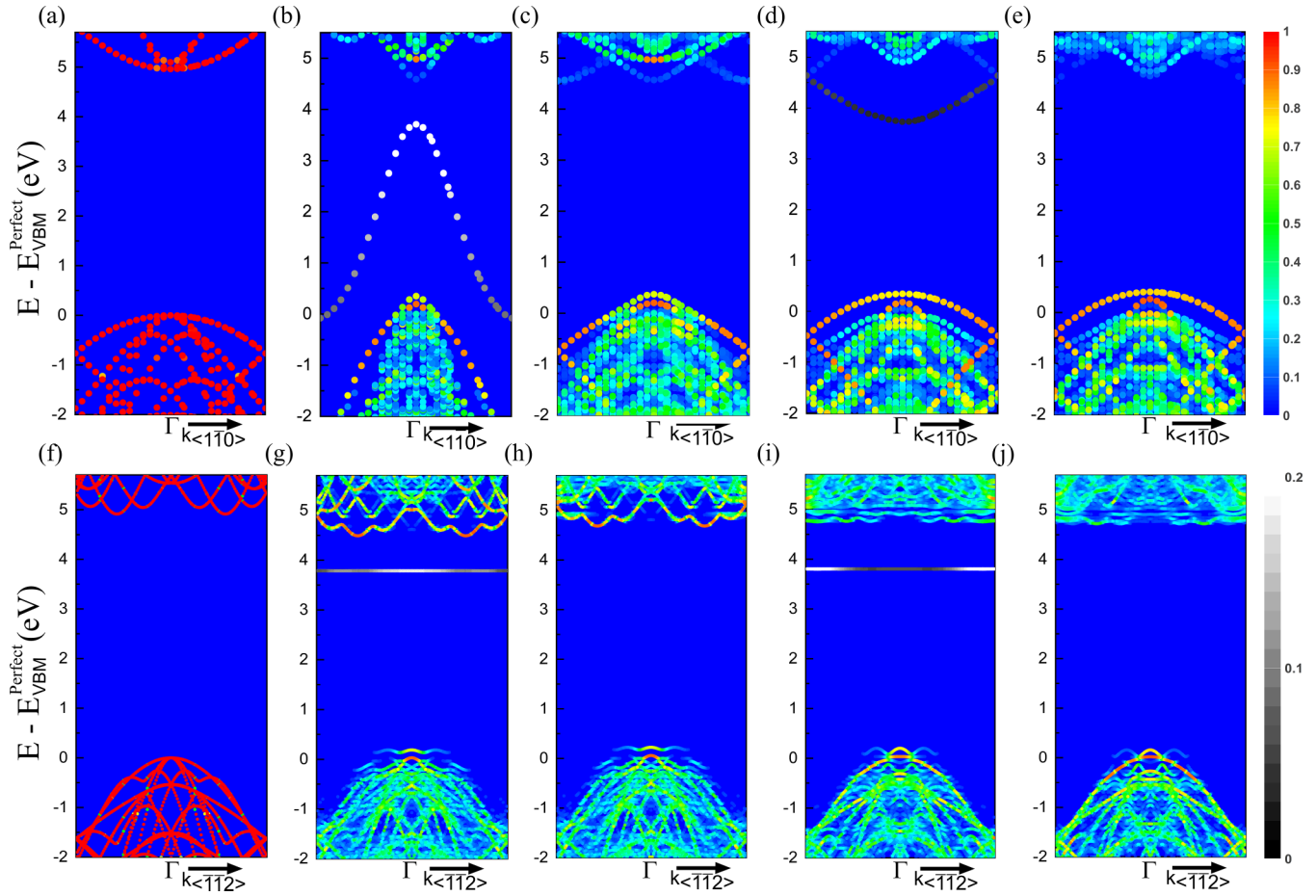
FIG. 4. Calculated electronic band structures for (a) perfect, (b) SP 30°, (c) DP 30°, (d) SP 90°, and (e) DP 90° dislocation dipole supercells, unfolded into the Brillouin zone of the primitive cell using the fold2Bloch code [35]. Top figures are the unfolded band structures along the dislocation line direction [1 $\bar{1}$ 0]. Bottom figures are the unfolded band structures along the Burgers vector direction [$\bar{1}$ $\bar{1}$ 2]. Color bars represent the Bloch spectral weight. Since the Bloch spectral weights of defects are in the range of [0,2], a gray scale color bar (bottom) is used for defect states that are well separated from the VB and CB of the SP 30° and 90° dislocation dipole supercells.

direction implying confinement of carriers in real space along this direction [Fig. 4(g)]. On the contrary, the half-filled defect state having metallic conductivity along the line direction is quite dispersive [Fig. 4(b)].

Figure 5 shows the partial DOS and the charge density plot along the dislocation line of the SP 30° partial dislocation.
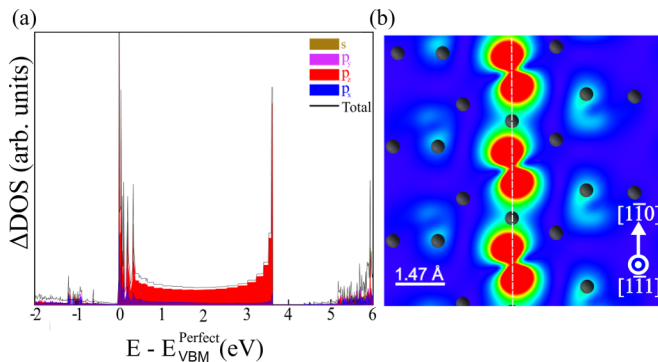

FIG. 5. (a) Orbital resolved partial density of states for SP 30°. (b) Charge density plot along the dislocation core of SP 30°. (Black balls represent the atoms lying on the glide plane.)

It is evident that these states largely consist of p_z orbitals; the charge density is localized along the line direction showing an array of overlapping p_z orbitals. Heavily localized charge density along the dislocation line combined with the dispersive band structure, demonstrate that 1D conduction takes place along the line direction within atomically narrow channels. These 1D metallic bands exhibit a DOS reduction of $1/\sqrt{E}$ at the conduction-band-like bottom, and vice versa, at the valence-band-like top of the band. Similar ideal 1D Fermi gases have been previously generated using scanning tunneling microscopy to arrange metallic atoms into chains; however, they degrade quickly on a surface [38]. Our results suggest that ideal quantum wires made from naturally occurring line defects in wide band gap materials may overcome these limitations.

Next, we quantify the carrier effective masses in the directions along and perpendicular to the dislocation line by calculating the effective masses in both directions. When there exists a localization, the effective mass approximation is not valid. However, we have already shown that the dangling bond wave functions extending along the dislocation line are heavily delocalized in that direction for SP 30°. Therefore, we compute the effective masses of carriers within the defect

TABLE II. Calculated effective mass values in units of m_0 along different crystallographic directions of bulk diamond in literature and in this work.

Parameter	Literature (bulk)	This work
$m_{hh}^{[111]}$	0.56 [39]	0.56
$m_{hh}^{[110]}$	2.12 [5], 1.34, 0.653 [40]	1.57
$m_{hh}^{[100]}$	0.40 [39]	
$m_{lh}^{[111]}$	0.53 [39]	0.28
$m_{lh}^{[110]}$	0.23 [39], 0.263 [40]	0.20
m_e^t	0.36 [39,41]	0.45
m_e^l	1.40 [39,41]	1.09

states along the line direction for SP 30° $m_{\mathrm{e,defect}}^{[1\bar{1}0]}$ to be equal to $0.15m_o$ at the Γ point and $m_{\mathrm{h,defect}}^{[1\bar{1}0]}$ to be equal to $0.17m_o$ at the Brillouin zone edges, using a simple curve fitting as explained in Sec. II.

Table II shows the calculated carrier effective masses in bulk diamond for reference, revealing that there is a far higher mobility of holes along the dislocation line direction compared to a perfect diamond crystal. Similarly, defect states of SP 90° dislocations are delocalized along the line direction but localized along the perpendicular direction [Figs. 4(d) and 4(i)]. The effective mass of carriers within the defect states along the line direction for SP 90° is calculated as $m_{\mathrm{e,defect}}^{[1\bar{1}0]}$ to be equal to $1.01m_o$ at the Γ point. When compared with reference band structures [Figs. 4(a) and 4(f)], no midgap states are observed along both line and perpendicular directions for any of the dislocations with DP reconstruction [Figs. 4(c), 4(h) 4(e), and 4(j)].

The unfolded band structures in Fig. 4 also provide insight into the anisotropic optical properties possible in dislocated diamond. Bulk diamond [Figs. 4(a) and 4(f)] exhibits a large indirect band gap of 4.95 eV. However, in the case of pure edge dislocations, (SP 90), a much smaller direct band gap of 3.21 eV is seen in our calculations. This implies the onset of optical absorption at 3.21 eV in dislocated diamond, and likely, luminescent emission of photons at, or slightly below this energy assuming some excitonic (e-h) coupling occurs. The literature on the optical properties of diamond is quite extensive, and it is widely reported that the broad blue band emission in diamond (centered at 2.8 eV) arises from dislocations [24–28]. Cathodoluminescence (CL) studies show blue emission in diamond arising exactly at the location of dislocations. Although CL can localize the luminescence to the vicinity of dislocations, it was not clear if radiative recombination was occurring in the core dislocation states themselves, or in the bulk diamond states around the dislocations. The latter could occur, for example, if point defects, or strain-generated carrier trapping and recombination pathways develop near the dislocations. CL excites a large population of hot carriers, well above the band edges

and as a result, cannot determine the absorption onset of the blue emission. But later, Iakoubovskii and Adriaenssens examined photoluminescence excitation (PLE) spectroscopy and identified an absorption onset for the blue band emission centered at 3.0 eV. These results demonstrated that excitation of photocarriers in the bulk states of diamond (≈ 5.5 eV) is not needed to drive the blue band emission. The band structure in Fig. 4(d) provides a straightforward explanation for the blue band CL and PLE emission data, indicating that the 2.8 eV emission band arises from band-to-band recombination in the core states of pure edge dislocations in diamond and with an absorption onset at 3.21 eV. We note that our calculated band gap values underestimate the experimental value, e.g., 4.95 eV compared to ≈ 5.5 eV for bulk diamnod. Therefore, while the numbers cannot be directly compared to the experimental measurements, the trend is in good agreement with the optical literature on diamond. Additionally, the anisotropy of the band structure also suggests an optical polarization axis with blue band emission parallel to the dislocation line, i.e., electric-dipole transitions along the dispersing band k vector. Again, literature backs up this prediction with the CL data of Kiflawi and Lang demonstrating $> 90\%$ polarization of blue band emission parallel to dislocation lines.

IV. CONCLUSIONS

Ground state electronic properties of the glide set of partial dislocations in diamond were calculated. We found that (1) the position and effective mass of dislocation-induced states depend heavily on the core structure, (2) only mixed dislocations with dangling bonds have metallic conductivity through half-filled gap states, (3) 1D conduction along the line direction of these dislocations is attributed to a chain of overlapping p_z orbitals forming a dispersive band along the line defect, (4) pure edge dislocations in diamond exhibit a direct band gap of 3.21 eV providing a theoretical explanation on the origin of the blue band emission in diamond, and (5) the DOS for the core states is that of an ideal 1D Fermi gas in both metallic and semiconducting dislocations. Consequently, dislocations with undercoordinated core atoms appear to be naturally formed 1D quantum wires. Core states of dislocations in wide band gap materials like diamond could be used as an active component in functional materials.

In this study, the geometry and electronic properties of ideal (straight and clean) partial dislocations are examined. Jogs, kinks, dislocation nodes, and point defect decorated dislocations can alter the effects on electronic structure, which should be investigated thoroughly in the future.

[1] A. Peaker and H. Grimmeiss, *Low-Dimensional Structures in Semiconductors: From Basic Physics to Applications* (Springer Science & Business Media, New York, 2013).

[2] A. Nakamura, K. Matsunaga, J. Tohma, T. Yamamoto, and Y. Ikuhara, Nat. Mater. **2**, 453 (2003).

[3] Y. Ikuhara, Prog. Mater. Sci. **54**, 770 (2009).

[4] Y. Tokumoto, S.-i. Amma, N. Shibata, T. Mizoguchi, K. Edagawa, T. Yamamoto, and Y. Ikuhara, J. Appl. Phys. **106**, 124307 (2009).

[5] S.-i. Amma, Y. Tokumoto, K. Edagawa, N. Shibata, T. Mizoguchi, T. Yamamoto, and Y. Ikuhara, Appl. Phys. Lett. **96**, 193109 (2010).

[6] I. Sugiyama, N. Shibata, Z. Wang, S. Kobayashi, T. Yamamoto, and Y. Ikuhara, Nat. Nanotechnol. **8**, 266 (2013).

[7] W. Zhou, X. Dai, T.-M. Fu, C. Xie, J. Liu, and C. M. Lieber, Nano Lett. **14**, 1614 (2014).

[8] W. Shockley, in *Physical Review* (American Physical Society, College Park, 1953), Vol. 91, p. 228.

[9] W. T. Read, Jr., London Edinburgh Philos. Mag. J. Sci. **45**, 775 (1954).

[10] R. Labusch and W. Schröter, Dislocations in Solids **5**, 127 (1980).

[11] R. Broudy, Adv. Phys. **12**, 135 (1963).

[12] R. L. Bell, R. Latkowski, and A. F. W. Willoughby, J. Mater. Sci. **1**, 66 (1966).

[13] J. R. Patel and P. E. Freeland, Phys. Rev. Lett. **18**, 833 (1967).

[14] H. Alexander and P. Haasen, in *Solid State Physics* (Elsevier, New York, 1969), Vol. 22, pp. 27–158.

[15] D. B. Holt and B. G. Yacobi, *Extended Defects in Semiconductors: Electronic Properties, Device Effects and Structures* (Cambridge University Press, Cambridge, UK, 2007).

[16] C. Claeys and E. Simoen, *Extended Defects in Germanium: Fundamental and Technological Aspects* (Springer, New York, 2009).

[17] R. Jones, J. Phys., Colloq. **40**, C6 (1979).

[18] S. Marklund and W. Yong-Liang, Solid State Commun. **82**, 137 (1992).

[19] Wang Yong-liang, Phys. Rev. B **40**, 5669 (1989).

[20] K. Lodge, A. Lapiccirella, C. Battistoni, N. Tomassini, and S. Altmann, Philos. Mag. A **60**, 643 (1989).

[21] R. E. Laukkonen, H. Biddel, and R. Gallagher, *Preparing Humanity for Change and Artificial Intelligence: Learning to Learn as a Safeguard Against Volatility, Uncertainty, Complexity, and Ambiguity* (OECD Publishing, Washington, DC, 2019).

[22] L. Pizzagalli, I. Belabbas, J. Kioseoglou, and J. Chen, Phys. Rev. Mater. **2**, 064607 (2018).

[23] I. Belabbas, J. Chen, and G. Nouet, Phys. Status Solidi C **12**, 1123 (2015).

[24] I. Kiflawi and A. R. Lang, Philos. Mag. **30**, 219 (1974).

[25] S. J. Pennycook, L. M. Brown, and A. J. Craven, Philos. Mag. A **41**, 589 (1980).

[26] N. Yamamoto, J. C. H. Spence, and D. Fathy, Philos. Mag. B **49**, 609 (1984).

[27] J. Ruan, K. Kobashi, and W. J. Choyke, Appl. Phys. Lett. **60**, 3138 (1992).

[28] K. Iakoubovskii and G. J. Adriaenssens, Phys. Rev. B **61**, 10174 (2000).

[29] G. Kresse and J. Furthmüller, Phys. Rev. B **54**, 11169 (1996).

[30] G. Kresse and D. Joubert, Phys. Rev. B **59**, 1758 (1999).

[31] J. Heyd and G. E. Scuseria, J. Chem. Phys. **121**, 1187 (2004).

[32] L. Pizzagalli and P. Beauchamp, Philos. Mag. Lett. **88**, 421 (2008).

[33] P. M. Anderson, J. P. Hirth, and J. Lothe, *Theory of Dislocations* (Cambridge University Press, Cambridge, UK, 2017).

[34] S. Lany and A. Zunger, Modell. Simul. Mater. Sci. Eng. **17**, 084002 (2009).

[35] O. Rubel, A. Bokhanchuk, S. J. Ahmed, and E. Assmann, Phys. Rev. B **90**, 115202 (2014).

[36] A. T. Blumenau, R. Jones, T. Frauenheim, B. Willems, O. I. Lebedev, G. Van Tendeloo, D. Fisher, and P. M. Martineau, Phys. Rev. B **68**, 014115 (2003).

[37] A. T. Blumenau, M. I. Heggie, C. J. Fall, R. Jones, and T. Frauenheim, Phys. Rev. B **65**, 205205 (2002).

[38] N. Nilius, T. M. Wallis, and W. Ho, Science **297**, 1853 (2002).

[39] H. Löfås, A. Grigoriev, J. Isberg, and R. Ahuja, AIP Adv. **1**, 032139 (2011).

[40] I. Akimoto, Y. Handa, K. Fukai, and N. Naka, Appl. Phys. Lett. **105**, 032102 (2014).

[41] M. Willatzen, M. Cardona, and N. E. Christensen, Phys. Rev. B **50**, 18054 (1994).